Atomic structure of solute clusters in Al–Zn–Mg alloys

A. Lervik[a], E. Thronsen[a], J. Friis[a,b], C.D. Marioara[b], S. Wenner[a,b], A. Bendo[c], K. Matsuda[c], R. Holmestad[a,*], S.J. Andersen[b]

[a] Department of Physics, Norwegian University of Science and Technology (NTNU), Trondheim N-7491, Norway
[b] SINTEF Industry, Trondheim, N-7465, Norway
[c] Graduate School of Science and Engineering, University of Toyama, 3190 Gofuku, Toyama 930-8555, Japan

ABSTRACT

Scanning transmission electron microscopy imaging of Al–Zn–Mg alloys has provided new information on the atomic structures of solute rich clusters forming from a supersaturated solid solution at low temperatures. A unique unit of high Zn/Mg ratio is the fundamental cluster building block. The unit is essentially a partial substitution by Mg and Zn on the cubic aluminium cell and its surrounding truncated cube octahedral shell. A simple set of principles based on Frank–Kasper structures describes how the basic units arrange with respect to each other to form larger clusters. Density functional theory calculations, atom probe tomography and simulated diffraction patterns support the proposed atomic models. The results provide new insight into the very early stages of age-hardening in aluminium alloys.

1. Introduction

The age-hardenable Al–Zn–Mg (7xxx) alloys are important in the transportation industry, due to properties such as good formability and high strength-to-weight ratio [1,2]. Prior to hardening, a high temperature solution heat treatment (SHT) is required to dissolve the solute atoms, followed by a quench to room temperature leading to a supersaturated, metastable solid solution consisting of solute elements and vacancies. By keeping the material at room temperature, the hardness will gradually increase [3]. This effect is called 'natural ageing (NA)' and is caused by solute atoms aggregating to clusters on the face centered cubic (fcc) aluminium lattice. The solute clusters act as small obstacles for dislocation movements during plastic deformation and contribute to strength.

Clusters with periodic ordering are referred to as 'Guinier–Preston (GP) zones', after their discoverers in 1938 [4,5]. In Al–Zn–Mg alloys, two types of GP-zones have been suggested: GP(I) related to solute rich clusters [6–10], and GP(II) related to vacancy rich clusters [6–12]. Earlier studies have suggested that both play key roles during the subsequent artificial ageing (AA) stage (120–200 °C), especially in initiating the formation of the coherent, hardening precipitate structure η' (MgZn$_2$) [6,13–18]. GP(I) zones have been found to exist even after longer ageing times [6,9,19,20]. The GP(II) zones are suggested as possible precursors

of the metastable η' precipitate [6,9]. However, the transformation from clusters to precipitates are not understood [12].

This work focuses on the structure of the solute rich GP(I) clusters formed at low temperature, previously reported in studies using transmission electron microscopy (TEM) [8,21–23], X-ray diffraction (XRD) [11,24–26] and positron annihilation spectroscopy (PAS) [11,27]. Up till now, a simple anti-phase ordering of solute has been proposed based on diffraction patterns acquired from large regions [8]. This work shows that the ordering is of a fundamentally different kind, and uncovers the atomic structure of the GP(I) zones with support from experimental techniques, simulations and calculations.

2. Material and methods

2.1. Materials

The data in this work has been obtained from two Al–Zn–Mg alloys. An industrial alloy (in at.%: 0.08% Fe, 1.42% Mg, 0.08% Si, 2.98% Zn and 0.04% Zr), labelled Alloy #1, was air cooled after extrusion and left naturally ageing for 17 years. A high purity lab-cast alloy (in at.%: 1.89% Mg and 3.49% Zn), labelled Alloy #2, was SHT at 475 °C for 1 h before it was quenched into water and left for NA. A group of samples were directly artificially aged at 150 °C, while some were artificially aged at 120 °C after 4 days of NA. The Vickers hardness (HV0.1) curve for Alloy #2 obtained during natural ageing reaches a hardness of ∼ 110 after ∼ 10 days. This does not

increase significantly with further natural ageing times. A similar hardness value is obtained after 4 days natural ageing and 8 min artificial ageing at 120 °C. Hardness curves are shown in Supplementary Fig. 1. Alloy #1 naturally aged for 17 years had a hardness value of 107 ± 11.

2.2. Transmission electron microscopy

TEM specimens were prepared by grinding bulk samples with SiC abrasive paper to ~ 60 μm foil thickness, punched into 3 mm discs and thereafter electropolished with a Struers TenuPol-5 machine using an electrolyte mixture of 1/3 HNO_3 and 2/3 C_3CH_3OH at temperatures between -30 and -20 °C and an applied potential of 20 V. High-resolution high-angle annular dark field (HAADF)-scanning transmission electron microscopy (STEM) images were acquired using an image- and probe Cs-corrected JEOL ARM200CF operated at 200 kV with convergence semi-angle and inner collector angle 28 mrad and 48 mrad, respectively. Smart Align (HREM research) was used in the acquisition, which involves acquiring a stack of successive low-dose images and afterwards aligning them to correct both rigid- and non-rigid scan distortions [28].

2.3. Atom probe tomography

Samples for atom probe tomography (APT) were prepared according to the conventional focused ion beam (FIB) lift-out method [29], using a FEI Helios G2 dual-beam instrument. The tips were oriented along the [001] direction and sharpened to apex diameters of <50 nm, finishing with a 5 kV Ga$^+$ ion beam. APT was performed with a Cameca LEAP 5000XS in voltage pulse mode, with the sample cooled to 50 K. A volume of 20 million atoms was evaporated with a pulse fraction of 25%, a pulse rate of 500 kHz, and 0.3% of the pulses leading to a detected atom. A detection efficiency of 77% was assumed in the data reconstruction. Poles and lattice spacings in the [001] directions were visible, allowing a fit of the image compression factor and field factor to obtain the correct scaling in all directions. The maximum separation algorithm was used [30], with clusters defined by 3rd nearest neighbor solutes being closer than $d_{max} = 0.53$ nm and the minimum size of clusters being $N_{min} = 80$ atoms. This maximizes the ratio of real to random identified clusters. Enveloping and erosion of 0.53 nm were used to define the cluster-matrix interface and improve composition quantification [30]. The cluster radius was estimated using the radius of gyration in the (non-aberrated) z direction multiplied by a shape factor. Since the chemical composition is averaged over a large number of small clusters, the statistical deviation is expected to be large and is used as an error estimate. Expected measurement errors include detection efficiency errors (the average error is roughly 1% in compositional fraction), uneven chemical distributions due to crystallographic poles, as well as background events. All these are random errors and are reflected in the statistically determined error.

2.4. Density functional theory

The density functional theory (DFT) calculations of the formation enthalpies for the structures were performed at 0 K with the Vienna Ab initio Simulation Package (VASP) [31,32], using the Perdew–Burke–Ernzerhof (PBE) gradient approximation [33]. A gamma-centred k-point mesh was used in all calculations with a plane wave energy cut-off above 400 eV and a maximal k-point distance of 0.18 Å^{-1}. The Methfessel–Paxton method [34] of 1st order was applied for atomic position relaxations with maximum force of 0.001 eV/Å and a smearing factor of 0.2. For accurate energies, all relaxations were followed by a static calculation using

the tetrahedron method with Bloch corrections. The formation enthalpies for the different configurations were calculated as

$$\Delta H = E - \sum_i E_{X_i}, \qquad (1)$$

where E is the total energy of the configuration in question and i is an index running over all atoms in the structure. E_X is the energy of one element X, embedded in the matrix ($X = $ Al, Mg, Zn). For consistency E_X is calculated from bulk Al supercells of the same size as the configuration in question with a single Al substituted with X [14];

$$E_X = E_{XAl_{N-1}} - \frac{N-1}{N} E_{Al_N}, \qquad (2)$$

where N is the number of atoms in the supercell.

2.5. Diffraction pattern and image simulations

The nanobeam diffraction (NBD) patterns were simulated using the μSTEM simulation software in the position-averaged convergent beam electron diffraction (PACBED) mode [35]. Calculations were carried out on a 512 × 512 pixel mesh grid with 10 layers of Al unit cells surrounding the cluster model on each lateral side forming a supercell with dimensions approximately 97 × 97 Å to avoid wrap-around errors due to the Al-cluster interface. The probe forming aperture was set to 0.75 mrad to avoid overlap of the diffraction spots. The model was periodic in the z-direction and the simulations were carried out over a TEM sample thickness interval of 12–700 Å. For the HAADF-STEM image simulations, the MULTEM simulation software was used [36]. Calculations were carried out on a 1024 × 1024 pixel mesh grid using a supercell with lateral dimensions of approximately 40 × 40 Å and a thickness of approximately 405 Å. The convergence angle was set to 27.78 mrad and the inner and outer collection angles were 48 mrad and 206 mrad, respectively.

3. Results and discussion

3.1. Microstructure overview

Conventional bright field (BF)-TEM imaging along the [001] Al direction showed high densities of small (1–2 nm) clusters uniformly distributed within the Al matrix, as Fig. 1**a** demonstrates for Alloy #1. Fig. 1**b** shows the corresponding selected area diffraction pattern (SADP). Two types of diffraction spots appear between the Al reflections. The sharp diffraction spots (red circles) on the {100} and {110} positions in Fig. 1**b** originate from larger Al$_3$Zr dispersoids [37,38]. The diffuse spots (yellow triangles) originate from clusters and are a result of high densities combined with the different crystallographically equivalent orientations the clusters can have with the aluminium, while the spread in intensity is due to their small physical size. These spots have previously been associated with GP(I) zones [8–10,21,22,37,39–42]. Fig. 1**c** shows a HAADF-STEM image of clusters and Fig. 1**d** shows the corresponding fast Fourier transform (FFT). It has strong resemblance with the SADP in Fig. 1**b**. The diffuse, high-intensity spots at the {110} positions in Fig. 1**d** are artefacts caused by the TEM sample preparation (cf. Supplementary Information) and should not be confused with the clear diffraction from the Al$_3$Zr dispersoids (Fig. 1**b**). After 2 weeks and after 8 months natural ageing, as well as for 8 min ageing at 120 °C, Alloy #2 exhibits the same diffuse diffraction spots as Alloy #1 (Fig. 1) with only slight variations in intensities. This is shown in Supplementary Fig. 2.

3.2. Cluster statistics and composition by atom probe tomography

Fig. 2**a** shows the solute Mg and Zn atoms inside the defined clusters in an evaporated APT needle of Alloy #1 after 17 years
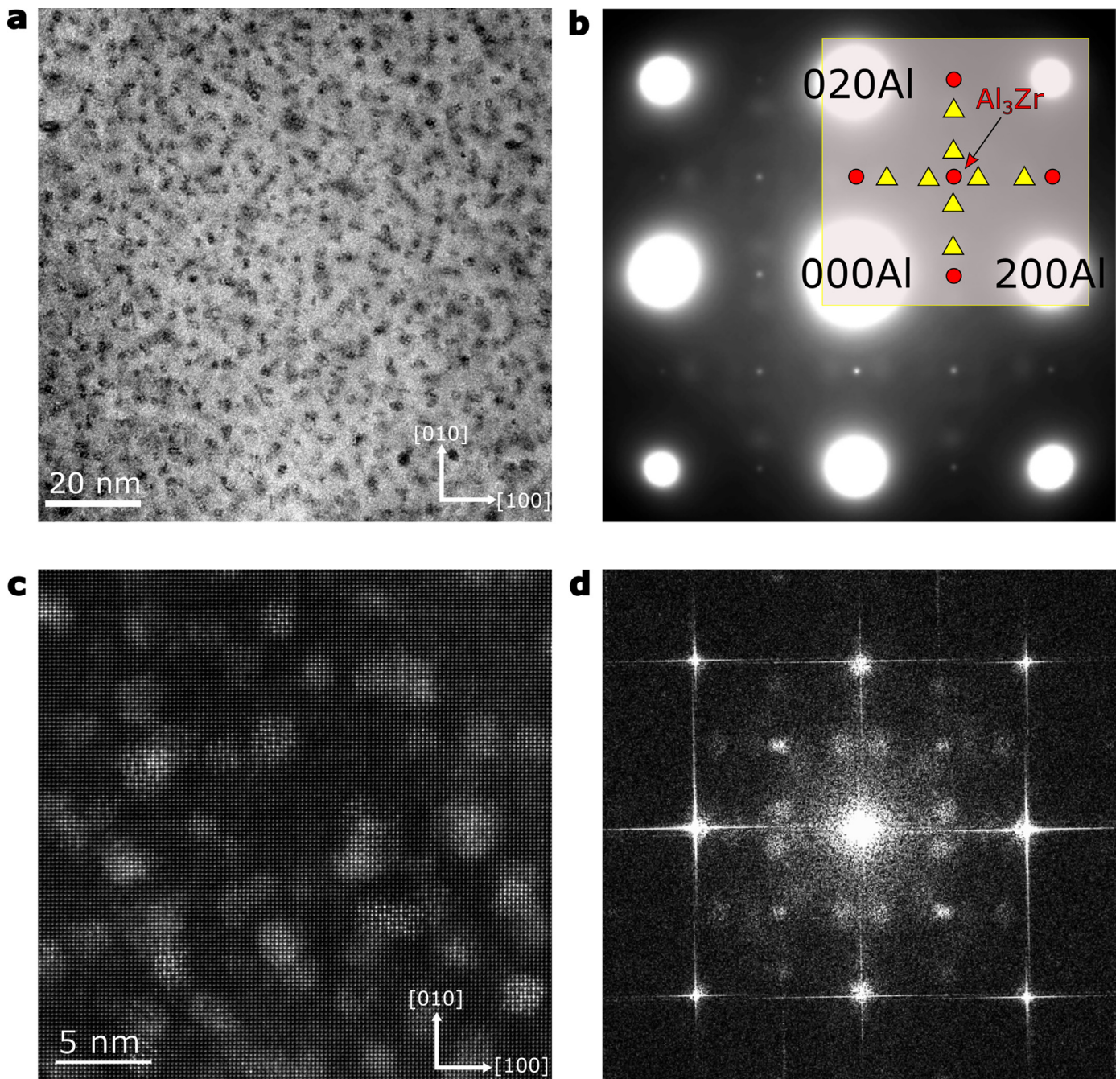
Fig. 1. Alloy #1 after 17 years of natural ageing, oriented along the [001] direction. **a**, BF-TEM image showing a high density of solute clusters (dark contrast). **b**, SADP with diffraction spots of Al_3Zr dispersoids and GP(I) zones, marked by circles and triangles, respectively. **c**, HAADF-STEM image clearly indicating ordering of solute on the fcc lattice. **d**, fast Fourier transform of **c** where the intensity in the forbidden {110} positions are due to a surface layer artefact.

natural ageing. As expected, dense co-clustering of Mg and Zn atoms is present. The composition of clusters as a function of the number of atoms within a cluster is shown in Fig. 2**b**. Clusters smaller than about 3 nm have a slightly lower level of Mg and Zn than the larger clusters. This is most likely an artifact of the evaporation field difference between clusters and the matrix, giving a local magnification effect [43]. The mean cluster radius is 1.90 nm, and the Zn/Mg ratio, which is shown as a function of the cluster diameter in Fig. 2**c**, has an average of 1.75. The average composition of clusters with a radius larger than 3 nm is 74.7 ± 0.2% Al, 16.8 ± 0.1% Zn, 8.5 ± 0.1% Mg (at.%). The measured Zn/Mg ratio is slightly higher than values reported in other APT studies [23,37,39,44–46]. However, these stud-

ies are not directly comparable as the alloys have different compositions and heat-treatments. Differences in natural ageing times can also affect the cluster composition [23]. In Cu-containing alloys, the ratio may be lower since Cu tends to substitute Zn positions [14,44]. The high amount of Al measured in the clusters is in agreement with other studies [37,44,46]. In the regions between the clusters, the Al matrix was found to contain 1.12 and 0.35 at.% Zn and Mg, respectively. The APT dataset gave an average nearest neighbour separation of 4.8 ± 0.9 nm and number density of clusters as approximately 3.35×10^{24} m^{-3}. The obtained values for mean size and number density are in correspondence with other studies using small-angle X-ray scattering (SAXS) [11,26,47].
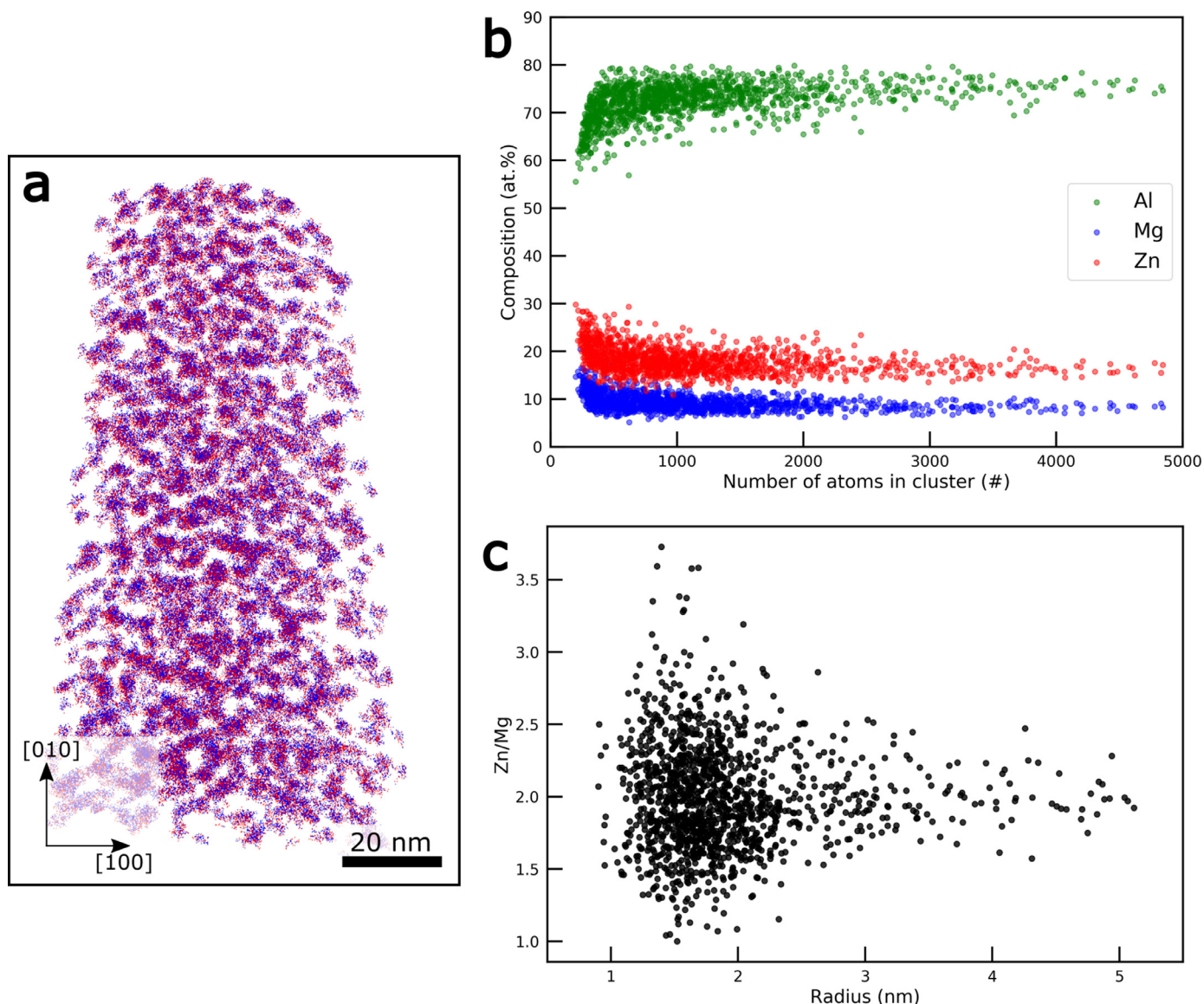
Fig. 2. a, Elemental map of solute atoms Mg (blue) and Zn (red) of clusters in Alloy #1 after 17 years NA, measured by atom probe tomography. **b**, composition of clusters shown against the number of atoms in each cluster. **c**, Zn/Mg ratio versus radius of the cluster. (For interpretation of the references to colour in this figure legend, the reader is referred to the web version of this article.)

3.3. Cluster units and their stacking principles

Both APT (Fig. 2**a**) and HAADF-STEM (Fig. 1**c**) indicate that the clusters are equiaxed. Along a ⟨100⟩ direction, approximately 1/3 of the non-overlapped clusters exhibits a clear atomic structure. Fig. 3**a** and **c** show two representative clusters. Based on the intensities and interatomic distances, suggested atomic motifs of Fig. 3**a** and **c** are given in **b** and **d**, respectively. Blue and red circles correspond to Al lattice columns with Mg and Zn substitutions, respectively. It can be seen that the atoms belonging to the cluster mostly adapt the Al lattice positions. The analysis demonstrates that the clusters may be simplified in terms of one single unit. This unit is identified by a unique high-intensity column situated at the centre where two rows of 5 bright columns along the lateral ⟨100⟩ Al directions intersect. This column is labelled as the 'Interstitial site' in Fig. 3. Together with the observation that the nearest four Zn columns of the centre are pushed slightly away (approximately 13%) from the ideal Al lattice, this indicates that the centre of the unit contains an interstitial atom relative to the fcc Al.

In the HAADF-STEM images along the [001] zone axis, the cluster unit has 4-fold symmetry. The solute arrangement compatible with these observations is a three-shell structure in the fcc lattice, centred on an Al cube with a possible interstitial. The inner shell is an octahedron formed by the six faces. The second shell is formed by the eight cube corners. The third shell is a truncated cube octahedron (TCO) of the 24 positions around the cube. Intensities in the images suggest that the shells have ideal compositions Zn_6, Mg_8 and Zn_{24}, respectively, with a common interstitial centre 'i'. This is illustrated in Fig. 3**e** and **f**. This cluster unit spans two Al-periods (8.1 Å). Thus, along the [001] direction the stacking is abbreviated by '[002]'. The TCO has six square and eight hexagonal faces, coinciding with the {100} and {111} Al planes, respectively, as shown in Fig. 3**e**. The 24 vertices are given by permutations of the lattice vector $\frac{1}{2}\langle 120 \rangle$ from the centre of the cube.

Individual clusters show variations in structure, as in Fig. 3**a** and **c**. However, they can always be explained in terms of the described TCO unit stacked according to three principles: [002], ⟨411⟩ and ⟨330⟩. The two last concerns the lateral plane, both with an
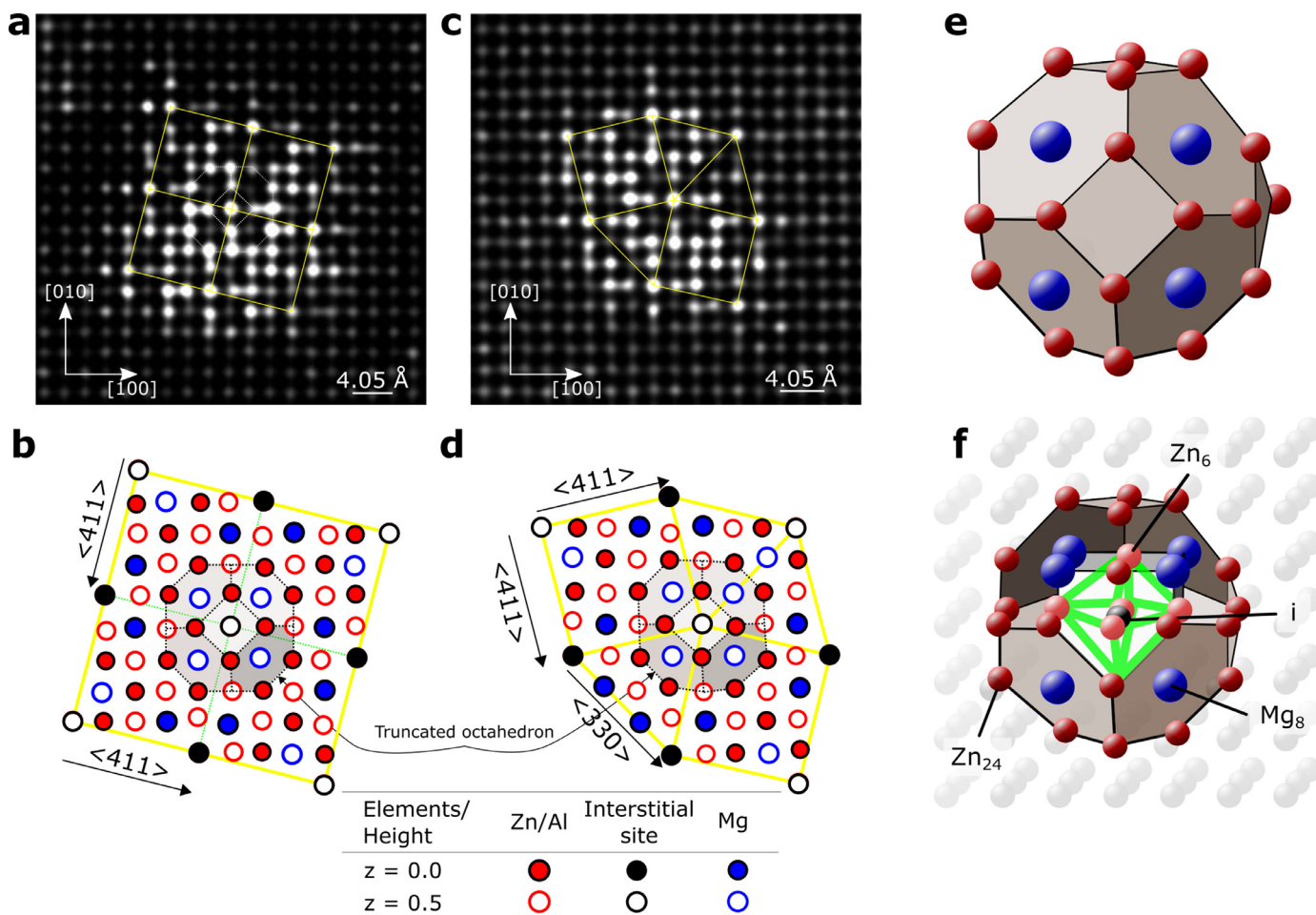
Fig. 3. a, c, Filtered HAADF-STEM images of two clusters. **b, d**, Suggested atomic column maps of **a** and **c**, showing the connection principles ($\langle 411 \rangle$, $\langle 330 \rangle$) between unit centres, denoted 'Interstital site'. **e**, TCO-shell with Zn on all vertices and Mg on corners. **f**, interior view of a cluster unit embedded in Al with an interstitial 'i'.

inter-distance of 8.59 Å as shown in Fig. 3, where the yellow lines connect the distinct 'Interstitial site' centres of the units. Experimental observations suggest that the most common lateral connection is $\langle 411 \rangle$. In Fig. 3a and b four units arrange in a $\langle 411 \rangle$ connected square. This is repeated in the viewing direction by the [002] connection. Fig. 3a and c show that the lateral connections form a pattern of squares and triangles, which is a σ-type Frank–Kasper ordering [48–50].

3.4. Density functional theory calculations

In order to elucidate the suggested structure, DFT calculations of cluster units embedded in $4 \times 4 \times 4$ Al cells (256 atoms) were conducted. We describe the unit by the nomenclature '$iZ_xM_yZ_z$', referring to the four constituents: an interstitial and three polyhedra (cf. Fig. 3f). The lower-case letter 'i' ($=$ a, z or m) indicates an interstitial centre (Al, Zn or Mg, respectively). If no interstitial is present, the character is omitted. Z_x ($x = 0, \ldots, 6$) indicates the number of Zn atoms on the cube faces, M_y ($y = 0, 8$) are the Mg atoms on the cube corners and Z_z ($z = 0, \ldots, 24$) is the number of Zn on the TCO shell. The maximum number of solute atoms in the cluster unit is 39 including the interstitial. Fig. 4 shows formation enthalpy versus pressure for a range of configurations of cluster units (cf. Supplementary Tables 1 and 2).

The DFT calculations show that the cluster units prefer high Zn/Mg ratios and the two Zn-containing shells filled by only Zn. Fig. 4 shows that a fully occupied TCO (Z_z, $z = 24$) is stabilising,

providing structures with 9 of the 11 lowest energies with Zn/Mg ratios above 3. Having both Zn shells fully occupied gives the best energies, which can be seen by considering the Mg-free series: $Z_0M_0Z_{12} \rightarrow Z_0M_0Z_{24} \rightarrow Z_6M_0Z_{24}$. This also shows that pressure falls with increased Zn concentration. Pressure represents the misfit volume compared to a supercell only containing Al but is not directly linked to energy: an interstitial ($zZ_6M_0Z_{24}$) improves pressure, but gives more unfavourable formation enthalpy. An interstitial Zn in $Z_0M_0Z_{12}$ ($zZ_6M_0Z_{12}$) is directly unfavourable. Thus, an interstitial is preferred for a Mg-cube (Mg_8) and one filled polyhedron (Z_6 or Zn_{24}), but preferably both.

$Z_6M_0Z_0$ and $zZ_6M_0Z_0$ show that Zn on the faces of an Al cell is more favorable than remaining in arbitrary solid solution, but that an interstitial is unlikely. With Mg on corners ($Z_6M_8Z_0$) the cluster energy improves significantly and an interstitial ($zZ_6M_8Z_0$) becomes favorable. This indicates that the interstitials are consequences of the TCO and not nucleation points. With an interstitial in $Z_6M_8Z_{24}$, three configurations of $iZ_6M_8Z_{24}$ are obtained with similar and overall lowest formation enthalpies. Despite a higher Zn/Mg ratio, $zZ_3M_8Z_{24}$ and $zZ_6M_8Z_{12}$ have comparable formation enthalpies. The reason is likely due to lower symmetry, as the inner octahedron Z_3 conserves only one (3-fold) symmetry axis.

3.5. Stacking of cluster units

Having established that the three most energetically favourable cluster units are of type $iZ_6M_8Z_{24}$, they were subsequently used to investigate the stability of larger clusters. The two stacking
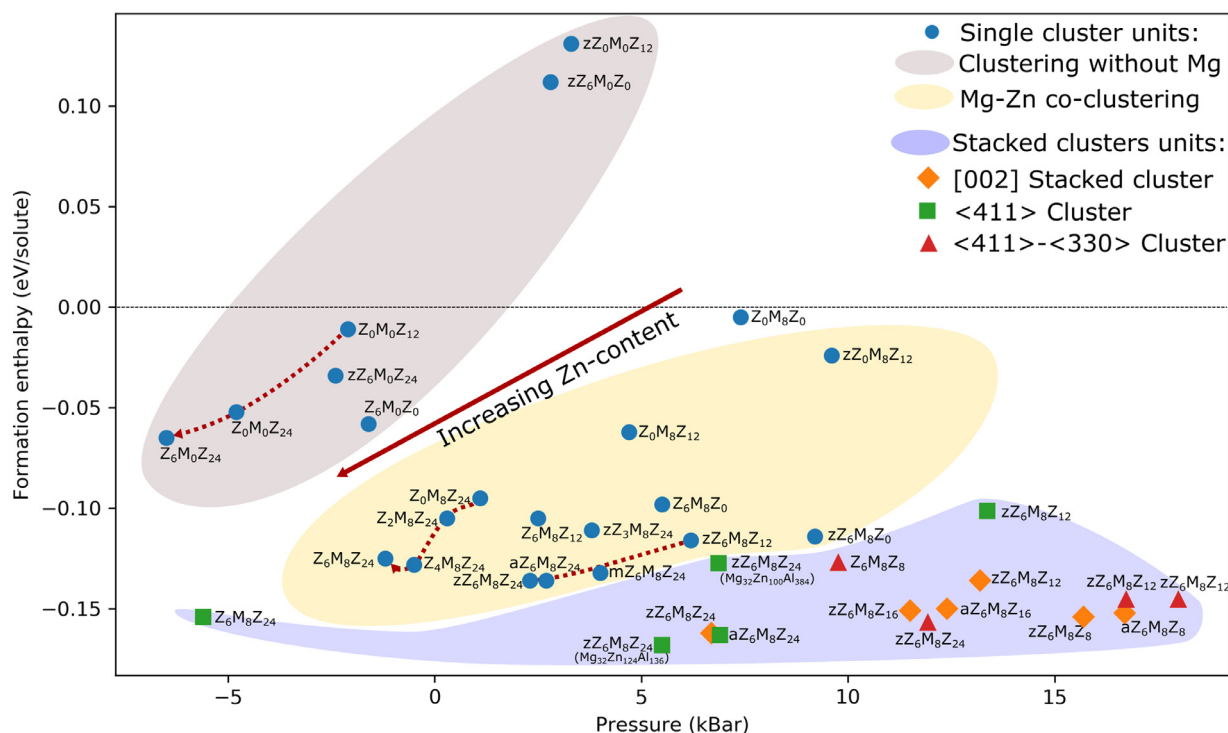
Fig. 4. DFT calculated formation enthalpy versus pressure for cluster structures with different Al, Zn, and Mg content embedded in aluminium matrix. Compositions refer to net content in single cluster units after stacking. Results demonstrate an advantage of high Zn content in the clusters. (Cf. Supplementary Tables 1 and 2 for detailed explanation of the structures.)
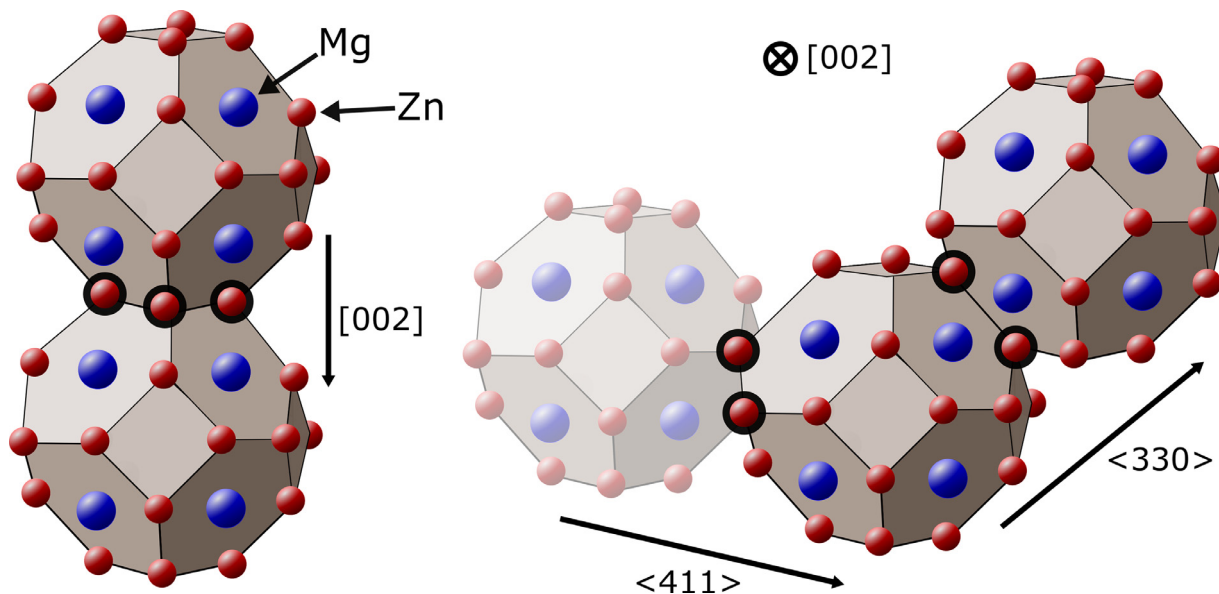

Fig. 5. Schematic illustration of the TCO unit stacking principles [002], $\langle 330 \rangle$ and $\langle 411 \rangle$ observed in the clusters. Note that the stacking causes certain atoms to be shared: two TCOs share 4, 2 and 2 positions, respectively, lowering the overall Zn/Mg ratio as compared to one TCO unit embedded in an Al matrix alone. The shared atoms are emphasised with black circles in the figure.

principles most frequently observed, [002] and $\langle 411 \rangle$, were used for the models, as shown in Fig. 5. A cluster of four units with $\langle 411 \rangle$ connections is shown in Fig. 6a. Two calculation supercells, $4 \times 4 \times 2$ and $6 \times 6 \times 2$ Al cells, were used for the [002] and the $\langle 411 \rangle$ stacked clusters, respectively. The calculations were done with Zn both fully and semi-occupied in the TCO shells. The results are marked by diamonds in Fig. 4 and labelled '[002] Stacked clusters' and '$\langle 411 \rangle$ Cluster'. Based on the calculations, it can be concluded that clusters stacked along [002] are more energetically favourable than single cluster units embedded in the Al matrix.

Moreover, by connecting the [002] stacked clusters in a $\langle 411 \rangle$ manner the lowest formation enthalpies are obtained for models containing an interstitial, which is in accordance with the analysis of HAADF-STEM images presented in Fig. 3.

The Zn/Mg ratio in the APT measurements was seen to approach 2 for larger clusters. In an infinite string of [002] connected units every unit shares 8 atomic positions. Thus, for the Zn completed cluster with Zn interstitial ($zZ_6M_8Z_{24}$), the number of Zn in the outer shell (Z_y) is reduced to 20, which results in an overall composition Mg_8Zn_{27}. The sharing of atoms due to
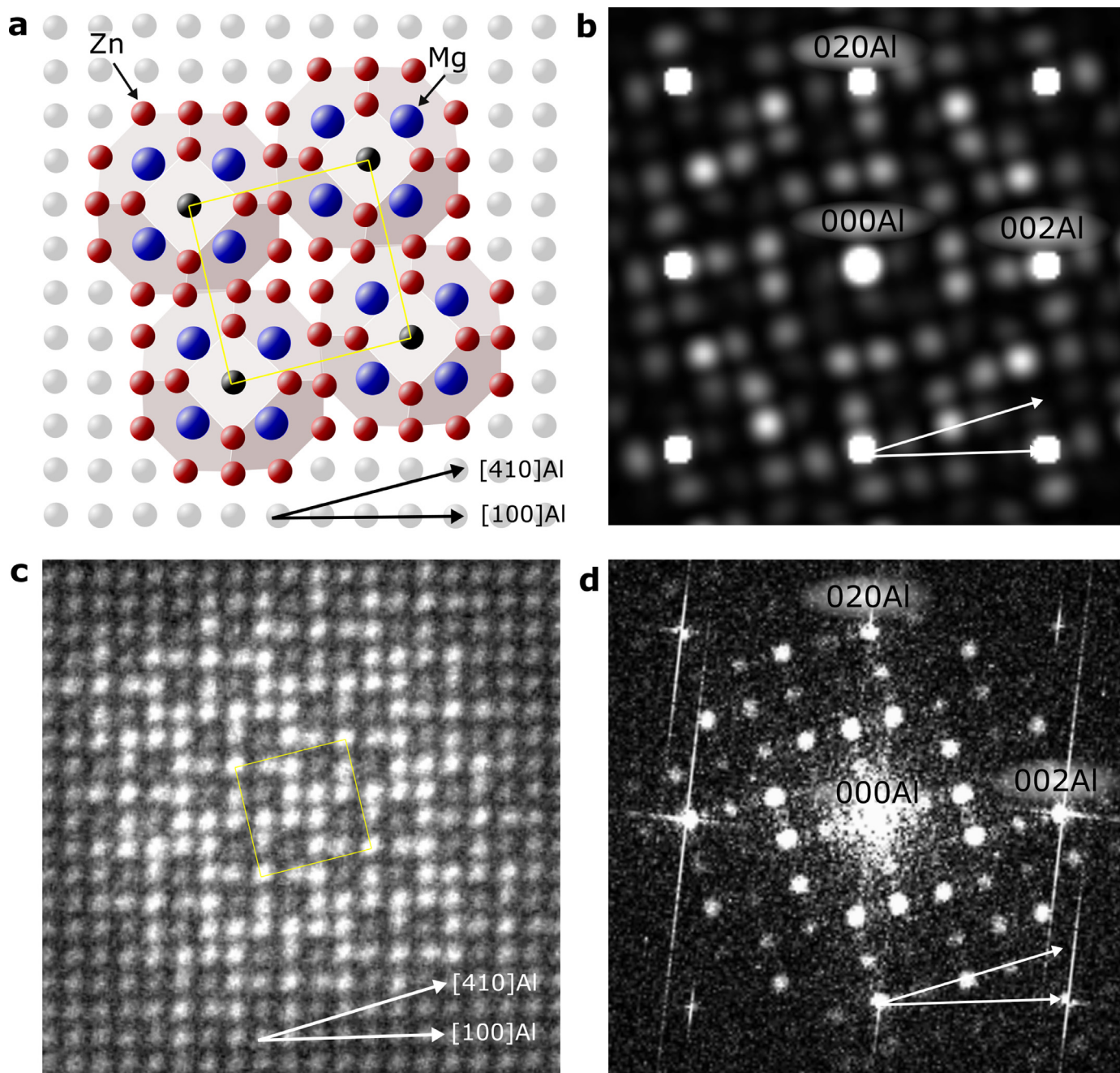
Fig. 6. a, [001] projection of $zZ_6M_8Z_{24}$ cluster units connected in a $\langle 411 \rangle$ square embedded in Al. **b**, Simulated NBD pattern of **a**. **c**, HAADF-STEM of a cluster in Alloy #2. **d**, FFT of **c**. The intensities of the simulated diffraction pattern in **b** match the intensities found in the corresponding FFT in **d**.

stacking is emphasised in Fig. 5 by black circles. Connecting four $zZ_6M_8Z_{24}$ units in a $\langle 411 \rangle$ square, means that for each unit 4 TCO positions are edge-shared. Therefore, the cluster $zZ_6M_8Z_{24}$ in an infinite stack of rings shares 12 atoms with neighbours and 'reduces' to $zZ_6M_8Z_{18}$ (Mg_8Zn_{25}). This Zn/Mg ratio (3.1) is still high compared to APT measurements. Although the calculations showed that single clusters prefer high Zn/Mg ratios, this suggests that the TCO and/or inner octahedron contain Al. HAADF-STEM image simulations (Supplementary Fig. 4.) support this: the intensity of the atomic columns belonging to the TCO and octahedron varies in the real images, whereas in the simulated image the intensity is constant due to constant amount of Zn in each column. Our models overestimate the Zn content as the atomic columns in the cluster-matrix interface in the simulations are consistently brighter than

in the experimental images. Phases taking Frank–Kasper structures are known to have flexible compositions [50]. The APT data and simulated HAADF-STEM images suggest that the Zn shells contain substantial amounts of Al. Thus, we suggest that the TCO clusters start out with full shells and higher Zn/Mg ratios. The availability of Zn may be reduced during growth, meaning that the outer TCO shell may have a higher fraction of Al, as is supported by the DFT calculations and APT measurements.

In addition, some clusters were found to connect along the $\langle 330 \rangle$ directions, as exemplified in Fig. 3c. Models following this connection principle are marked as '$\langle 411 \rangle - \langle 330 \rangle$ Clusters' in Fig. 4 and the models consist of three single cluster units with one $\langle 330 \rangle$ connection and two $\langle 411 \rangle$ connections. For this stacking, the most favourable cluster is $zZ_6M_8Z_{24}$, again demonstrating that a

high Zn/Mg ratio is preferred. Furthermore, the higher pressure of the $\langle 411 \rangle - \langle 330 \rangle$ clusters compared to their $\langle 411 \rangle$ counterparts, suggests that they are less favourable. This is in accordance with our experimental observations.

3.6. Diffraction from a single cluster

The contribution from a single cluster to the weak SADP diffraction spots (cf. Fig. 1b), was investigated. Using the $\langle 411 \rangle$ connected $zZ_6M_8Z_{24}$ cluster with the lowest formation enthalpy, as shown embedded in the Al matrix in Fig. 6a, NBD patterns were simulated. A simulated NBD pattern for sample thickness, $t = 40$ Å, is given in Fig. 6b. Montages of diffraction patterns ranging from 4 to 320 monolayers (0.8 to 64 nm) are shown in Supplementary Figs. 5 and 6. NBD patterns were also simulated for clusters positioned at different heights within the TEM sample (Supplementary Fig. 7). In Fig. 6c, a 'Smart Aligned' [28] HAADF-STEM image of a $\langle 411 \rangle$ connected cluster is shown, acquired in Alloy #2 after 400 min artificial ageing (cf. Supplementary Fig. 1). By comparing the FFT of Fig. 6c and d with the simulated NBD pattern in Fig. 6b, a strong correlation, both in position and intensity is evident. Note that, although Alloy #2 has been artificially aged, clusters are still present. This is in accordance with previous studies [6,9,19,20,46].

The lower cluster symmetry along [001] relative to Al, is obvious in Fig. 6a. The cluster belongs to space group P41 (#76), with a 4-fold screw axis, which projects to a pure rotational axis. It means that the cluster, as well as the diffraction pattern, will reverse the rotation as viewed from the other side. By taking the average from the two orientations, the resultant diffraction pattern is similar to the SADP in Fig. 1b. This is shown in Supplementary Fig. 8.

3.7. Transformations

The hardening precipitates in the 7xxx system and the equilibrium phase MgZn$_2$ have similar structures [14,16], facilitating transformation to the latter. This work finds no structural similarities between the GP(I) clusters and the precipitates. The clusters can be nucleation sites for the precipitates, but are likely to dissolve once hardening precipitates are established to fuel further precipitate growth. Thus, a low formation enthalpy associated with a cluster may delay, rather than assist precipitation. Future work will investigate how effective the different clusters are in forming the hardening phases. Better control of clustering has potential benefits for improving mechanical properties. It should be noted that an interstitial in the TCO produces a vacancy in the surrounding matrix, which could make the cluster more costly to produce. In the calculations this is not accounted for. It has been suggested before that some form of Mg clustering surrounding a vacancy is crucial in the earliest stages [6,11]. The calculations indicate a pathway: (1) Six Zn atoms occupies the centers of the Al cell, (2) eight Mg atoms replace the corners, (3) an interstitial is produced by a jump from a side to the cell center and (4) The side center is replaced by another Zn atom, and produces a vacancy that may be trapped or escape into the matrix.

3.8. Relation to quasi-crystalline phases

The 7xxx alloy system is known for phases related to quasi-crystals (QC) [51]. The complex R-(Al,Zn)$_{49}$Mg$_{32}$ phase [52] is a so-called 1/1 approximant of the QC (cf. [53–55]) in addition to being a Frank–Kasper phase [50]. We therefore compared the molecular unit of R with the clusters. Both are shell-structures, but were found to differ fundamentally, both compositionally and structurally. It cannot be ruled out that the TCO relates to the QC, such as through a complex sharing, but this was beyond the scope of the current work.

4. Conclusion

To conclude, we have derived the structure of the clusters forming during natural ageing in Al–Zn–Mg alloys. They are solute orderings on the fcc aluminium and essentially Frank–Kasper σ-type structures. The orderings have been explained as stackings in terms of a near spherical solute-ordered unit. The unit is a three-layered shell structure around an Al unit cell, which can take up an interstitial during build-up: an octahedron formed by the six side centres, a cube with Mg on the eight corners and the immediate truncated cube octahedral shell with 24 atomic positions. The octahedron and the outer TCO shell are partially or fully occupied by Zn, while the interstitial can take all three species. The interstitial was found to be a product of the cluster rather than a nucleation point. Three stacking principles are sufficient to explain how the cluster unit builds larger clusters, which are all Frank–Kasper structures. The partial occupancy of Zn yields a range of different compositions with favourable energies, which is typical for Frank–Kasper orderings. We expect our result to be significant in further understanding and optimisation of age-hardening in aluminium alloys.

Author contribution

A.L., A.B., K.M., R.H. and S.J.A. conceived, designed and supervised the research. A.L. conducted the (S)TEM experiments. S.W. conducted the APT measurements and analysis. J.F. prepared the models and conducted the DFT modelling. E.T. conducted the image and diffraction simulations. S.J.A. and C.D.M. analysed the data and deduced the structure. A.L. and E.T. prepared the figures. A.L., E.T. and S.J.A wrote the manuscript with input from all the authors.

Data availability

The data used to produce this work is openly available from the Zenodo data archive repository at: https://doi.org/10.5281/zenodo.3988972.

Declaration of Competing Interest

The authors declare that they have no known competing financial interests or personal relationships that could have appeared to influence the work reported in this paper.

Acknowledgements

Supplementary material

Supplementary material associated with this article can be found, in the online version, at doi:10.1016/j.actamat.2020.116574.

References

[1] O. Jensrud, High strength aluminium alloys extrusions-A review of the thermo-mechanical-process in high performance profile manufacturing, Key Eng. Mater. 491 (2011) 11–18. 10.4028/www.scientific.net/KEM.491.11

[2] T. Dursun, C. Soutis, Recent developments in advanced aircraft aluminium alloys, Mater. Des. 56 (2014) 862–871, doi:10.1016/j.matdes.2013.12.002.

[3] E. Hornbogen, Hundred years of precipitation hardening, J. Light Metals 1 (2) (2001) 127–132, doi:10.1016/S1471-5317(01)00006-2.

[4] A. Guinier, Structure of age-hardened aluminium-copper alloys, Nature 142 (3595) (1938) 569–570, doi:10.1038/142569b0.

[5] G. Preston, LXXIV. The diffraction of X-rays by an age-hardening alloy of aluminium and copper. The structure of an intermediate phase, Lond. Edinb. Dublin Philos. Mag. J. Sci. 26 (178) (1938) 855–871, doi:10.1080/14786443808562177.

[6] H. Löffler, I. Kovács, J. Lendvai, Decomposition processes in Al–Zn–Mg alloys, J. Mater. Sci. 18 (1983) 2215–2240, doi:10.1007/BF00541825.

[7] G. Dlubek, R. Krause, O. Brümmer, F. Plazaola, Study of formation and reversion of Guinier–Preston zones in Al-4.5 at.%Zn-x at%Mg alloys by positrons, J. Mater. Sci. 21 (3) (1986) 853–858, doi:10.1007/BF01117364.

[8] L.K. Berg, J. Gjønnes, V. Hansen, X.Z. Li, M. Knutson-Wedel, G. Waterloo, D. Schryvers, L.R. Wallenberg, GP-zones in Al–Zn–Mg alloys and their role in artificial aging, Acta Mater. 49 (17) (2001) 3443–3451, doi:10.1016/S1359-6454(01)00251-8.

[9] V. Hansen, O.B. Karlsen, Y. Langsrud, J. Gjønnes, Precipitates, zones and transitions during aging of Al–Zn–Mg–Zr 7000 series alloy, Mater. Sci. Technol. 20 (2) (2004) 185–193, doi:10.1179/026708304225010424.

[10] J. Buha, R.N. Lumley, A.G. Crosky, Secondary ageing in an aluminium alloy 7050, Mater. Sci. Eng. 492 (1–2) (2008) 1–10, doi:10.1016/j.msea.2008.02.039.

[11] A. Dupasquier, R. Ferragut, M.M. Iglesias, M. Massazza, G. Riontino, P. Mengucci, G. Barucca, C.E. MacChi, A. Somoza, Hardening nanostructures in an AlZnMg alloy, Philos. Mag. 87 (22) (2007) 3297–3323, doi:10.1080/14786430701271959.

[12] T.-F. Chung, Y.-L. Yang, B.-M. Huang, Z. Shi, J. Lin, T. Ohmura, J.-R. Yang, Transmission electron microscopy investigation of separated nucleation and in-situ nucleation in AA7050 aluminium alloy, Acta Mater. 149 (2018) 377–387, doi:10.1016/j.actamat.2018.02.045.

[13] J. Gjønnes, C.J. Simensen, An electron microscope investigation of the microstructure in an aluminium-zinc-magnesium alloy, Acta Metall. 18 (8) (1970) 881–890, doi:10.1016/0001-6160(70)90016-7.

[14] C.D. Marioara, W. Lefebvre, S.J. Andersen, J. Friis, Atomic structure of hardening precipitates in an Al-Mg-Zn-Cu alloy determined by HAADF-STEM and first-principles calculations: Relation to η-MgZn2, J. Mater. Sci. 48 (10) (2013) 3638–3651, doi:10.1007/s10853-013-7158-3.

[15] A. Bendo, K. Matsuda, S. Lee, K. Nishimura, N. Nunomura, H. Toda, M. Yamaguchi, T. Tsuru, K. Hirayama, K. Shimizu, H. Gao, K. Ebihara, M. Itakura, T. Yoshida, S. Murakami, Atomic scale HAADF-STEM study of η′ and η₁ phases in peak-aged Al-Zn-Mg alloys, J. Mater. Sci. 53 (6) (2018) 4598–4611, doi:10.1007/s10853-017-1873-0.

[16] A. Lervik, C. Marioara, M. Kadanik, J. Walmsley, B. Milkereit, R. Holmestad, Precipitation in an extruded AA7003 aluminium alloy: Observations of 6xxx-type hardening phases, Mater. Des. 186 (2020) 108204, doi:10.1016/j.matdes.2019.108204.

[17] T.-F. Chung, Y.-L. Yang, M. Shiojiri, C.-N. Hsiao, W.-C. Li, C.-S. Tsao, Z. Shi, J. Lin, J.-R. Yang, An atomic scale structural investigation of nanometre-sized η precipitates in the 7050 aluminium alloy, Acta Mater. 174 (2019) 351–368, doi:10.1016/j.actamat.2019.05.041.

[18] A. Bendo, T. Maeda, K. Matsuda, A. Lervik, R. Holmestad, C.D. Marioara, K. Nishimura, N. Nunomura, H. Toda, M. Yamaguchi, K.-i. Ikeda, T. Homma, Characterisation of structural similarities of precipitates in Mg–Zn and Al–Zn–Mg alloys systems, Philos. Mag. 99 (21) (2019) 2619–2635, doi:10.1080/14786435.2019.1637032.

[19] H. Inoue, T. Sato, Y. Kojima, T. Takahashi, The temperature limit for GP zone formation in an Al–Zn–Mg alloy, Metall. Mater. Trans. A 12 (8) (1981) 1429–1434, doi:10.1007/BF02643687.

[20] C.K. Akuata, C. Altenbach, C. Schnatterer, P. Suwanpinij, C. Saiyasombat, D. Zander, Age hardening response of AA7108A investigated by means of Synchrotron-based X-ray Absorption Spectroscopy (XAS) measurements, Mater. Sci. Eng. 747 (September 2018) (2019) 42–52, doi:10.1016/j.msea.2019.01.052.

[21] X.J. Jiang, J. Taftø, B. Noble, B. Holme, G. Waterloo, Differential scanning calorimetry and electron diffraction investigation on low-temperature aging in Al–Zn–Mg alloys, Metall. Mater. Trans. A 31 (2) (2000) 339–348, doi:10.1007/s11661-000-0269-x.

[22] W. Sun, Y. Zhu, R. Marceau, L. Wang, Q. Zhang, X. Gao, C. Hutchinson, Precipitation strengthening of aluminum alloys by room-temperature cyclic plasticity, Science 363 (6430) (2019) 972–975, doi:10.1126/science.aav7086.

[23] J. Liu, R. Hu, Y. Zhang, D. Zhigang, W. Liu, Y. Zhu, G. Sha, Formation of solute nanostructures in an Al–Zn–Mg alloy during long-term natural aging, J. Alloys Compd. 821 (2019) 153572, doi:10.1016/j.jallcom.2019.153572.

[24] A. Deschamps, Y. Bréchet, F. Livet, Influence of copper addition on precipitation kinetics and hardening in Al–Zn–Mg alloy, Mater. Sci. Technol. 15 (9) (1999) 993–1000, doi:10.1179/026708399101506832.

[25] A. Deschamps, M. Niewczas, F. Bley, Y. Brechet, J.D. Embury, L.L. Sinq, F. Livet, J.P. Simon, Low-temperature dynamic precipitation in a supersaturated Al–Zn–Mg alloy and related strain hardening, Philos. Mag. A 79 (10) (1999) 2485–2504, doi:10.1080/01418619908214295.

[26] P. Schloth, J.N. Wagner, J.L. Fife, A. Menzel, J.-M. Drezet, H. Van Swygenhoven, Early precipitation during cooling of an Al–Zn–Mg–Cualloy revealed by *in situ* small angle X-ray scattering, Appl. Phys. Lett. 105 (10) (2014) 101908, doi:10.1063/1.4894768.

[27] R. Ferragut, A. Somoza, A. Tolley, Microstructural evolution of 7012 alloy during the early stages of artificial ageing, Acta Mater. 47 (17) (1999) 4355–4364, doi:10.1016/S1359-6454(99)00315-8.

[28] L. Jones, H. Yang, T.J. Pennycook, M.S.J. Marshall, S. Van Aert, N.D. Browning, M.R. Castell, P.D. Nellist, Smart slign - a new tool for robust non-rigid registration of scanning microscope data, Adv. Struct. Chem. Imaging 1 (1) (2015) 8, doi:10.1186/s40679-015-0008-4.

[29] T.J. Prosa, D.J. Larson, Modern focused-ion-beam-based site-specific specimen preparation for atom probe tomography, Microsc. Microanal. 23 (2) (2017) 194–209, doi:10.1017/S1431927616012642.

[30] E.A. Jägle, P.-P. Choi, D. Raabe, The maximum separation cluster analysis algorithm for atom-probe tomography: parameter determination and accuracy, Microsc. Microanal. 20 (6) (2014) 1662–1671, doi:10.1017/S1431927614013294.

[31] G. Kresse, J. Hafner, Ab initio molecular dynamics for open-shell transition metals, Phys. Rev. B 48 (1993) 13115–13118, doi:10.1103/PhysRevB.48.13115.

[32] G. Kresse, D. Joubert, From ultrasoft pseudopotentials to the projector augmented-wave method, Phys. Rev. B 59 (1999) 1758–1775, doi:10.1103/PhysRevB.59.1758.

[33] J.P. Perdew, K. Burke, M. Ernzerhof, Generalized gradient approximation made simple, Phys. Rev. Lett. 77 (1996) 3865–3868, doi:10.1103/PhysRevLett.77.3865.

[34] M. Methfessel, A.T. Paxton, High-precision sampling for Brillouin-zone integration in metals, Phys. Rev. B 40 (1989) 3616–3621, doi:10.1103/PhysRevB.40.3616.

[35] L.J. Allen, A.J. D'Alfonso, S.D. Findlay, Modelling the inelastic scattering of fast electrons, Ultramicroscopy 151 (2015) 11–22, doi:10.1016/j.ultramic.2014.10.011.

[36] I. Lobato, D.V. Dyck, MULTEM: a new multislice program to perform accurate and fast electron diffraction and imaging simulations using graphics processing units with CUDA, Ultramicroscopy 156 (2015) 9–17.

[37] K. Stiller, P.J. Warren, V. Hansen, J. Angenete, J. Gjønnes, Investigation of precipitation in an Al-Zn-Mg alloy after two-step ageing treatment at 100° and 150°C, Mater. Sci. Eng.: A 270 (1) (1999) 55–63, doi:10.1016/S0921-5093(99)00231-2.

[38] A. Cassell, J. Robson, C. Race, A. Eggeman, T. Hashimoto, M. Besel, Dispersoid composition in zirconium containing Al–Zn–Mg–Cu (AA7010) aluminium alloy, Acta Mater. 169 (2019) 135–146, doi:10.1016/j.actamat.2019.02.047.

[39] G. Sha, A. Cerezo, Early-stage precipitation in Al–Zn–Mg–Cu alloy (7050), Acta Mater. 52 (15) (2004) 4503–4516, doi:10.1016/j.actamat.2004.06.025.

[40] J. Chen, L. Zhen, S. Yang, W. Shao, S. Dai, Investigation of precipitation behavior and related hardening in AA 7055 aluminum alloy, Mater. Sci. Eng. 500 (1–2) (2009) 34–42, doi:10.1016/j.msea.2008.09.065.

[41] D. Liu, B. Xiong, F. Bian, Z. Li, X. Li, Y. Zhang, Q. Wang, G. Xie, F. Wang, H. Liu, Quantitative study of nanoscale precipitates in Al–Zn–Mg–Cu alloys with different chemical compositions, Mater. Sci. Eng. 639 (2015) 245–251, doi:10.1016/j.msea.2015.04.104.

[42] K. Matsuda, A. Kawai, K. Watanabe, S. Lee, C.D. Marioara, S. Wenner, K. Nishimura, T. Matsuzaki, N. Nunomura, T. Sato, R. Holmestad, S. Ikeno, Extra electron diffraction spots caused by fine precipitates formed at the early stage of aging in Al–Mg–X (X=Si, Ge, Zn)-Cu alloys, Mater. Trans. 58 (2) (2017) 167–175, doi:10.2464/jilm.67.186.

[43] T. Philippe, M. Gruber, F. Vurpillot, D. Blavette, Clustering and local magnification effects in atom probe tomography: a statistical approach, Microsc. Microanal. 16 (5) (2010) 643–648, doi:10.1017/S1431927610000449.

[44] K. Hono, N. Sano, T. Sakurai, Quantitative atom-probe analysis of some aluminum alloys, Surf. Sci. 266 (1) (1992) 350–357, doi:10.1016/0039-6028(92)91045-D.

[45] S.K. Maloney, K. Hono, I.J. Polmear, S.P. Ringer, The chemistry of precipitates in an aged Al-2.1Zn-1.7Mg at.% alloy, Scr. Mater. 41 (10) (1999) 1031–1038, doi:10.1016/S1359-6462(99)00253-5.

[46] Y.L. Wang, Y.Y. Song, H.C. Jiang, Z.M. Li, D. Zhang, L.J. Rong, Variation of nanoparticle fraction and compositions in two-stage double peaks aging precipitation of Al–Zn–Mg alloy, Nanoscale Res. Lett. 13 (2018) 131, doi:10.1186/s11671-018-2542-1.

[47] R.K. Gupta, A. Deschamps, M.K. Cavanaugh, S.P. Lynch, N. Birbilis, Relating the early evolution of microstructure with the electrochemical response and mechanical performance of a Cu-rich and Cu-lean 7xxx aluminum alloy, J. Electrochem. Soc. 159 (11) (2012) C492–C502, doi:10.1149/2.062211jes.

[48] F.C. Frank, J.S. Kasper, Complex alloy structures regarded as sphere packings. I. Definitions and basic principles, Acta Crystallogr. 11 (3) (1958) 184–190, doi:10.1107/S0365110X58000487.

[49] F.C. Frank, J.S. Kasper, Complex alloy structures regarded as sphere packings. II. Analysis and classification of representative structures, Acta Crystallogr. 12 (7) (1959) 483–499, doi:10.1107/S0365110X59001499.

[50] J.-M. Joubert, J.-C. Crivello, Non-stoichiometry and calphad modeling of Frank–Kasper phases, Appl. Sci. 2 (3) (2012) 669–681, doi:10.3390/app2030669.

[51] D. Shechtman, I. Blech, D. Gratias, J.W. Cahn, Metallic phase with long-range orientational order and no translational symmetry, Phys. Rev. Lett. 53 (1984) 1951–1953, doi:10.1103/PhysRevLett.53.1951.

[52] G. Bergman, J.L.T. Waugh, L. Pauling, The crystal structure of the metallic phase $Mg_{32}(Al,Zn)_{49}$, Acta Crystallogr. 10 (4) (1957) 254–259, doi:10.1107/S0365110X57000808.

[53] T. Takeuchi, U. Mizutani, Electronic structure, electron transport properties, and relative stability of icosahedral quasicrystals and their 1/1 and 2/1 ap-proximants in the Al-Mg-Zn alloy system, Phys. Rev. B 52 (1995) 9300–9309, doi:10.1103/PhysRevB.52.9300.

[54] J. Hafner, M. Krajčí, Localized modes and topological frustration in rational ap-proximants to quasicrystals, Phys. Rev. B 47 (1993) 1084–1087, doi:10.1103/PhysRevB.47.1084.

[55] M. Krajčí, J. Hafner, Structure and stability of quasicrystals: modulated tiling models, Phys. Rev. B 46 (1992) 10669–10685, doi:10.1103/PhysRevB.46.10669.